Scaling factors for channel width variations in tree-like flow field patterns for polymer electrolyte membrane fuel cells - An experimental study

Marco Sauermoser [a,*], Bruno G. Pollet [b,c], Natalya Kizilova [d,a],
Signe Kjelstrup [a]

[a] PoreLab, Department of Chemistry, Norwegian University of Science and Technology, NTNU, Trondheim, Norway
[b] Department of Energy and Process Engineering, Norwegian University of Science and Technology, NTNU, Trondheim, Norway
[c] South African Institute for Advanced Materials Chemistry (SAIAMC), University of the Western Cape, South Africa
[d] Warsaw University of Technology, Institute of Aviation and Applied Mechanics, Warsaw, Poland

HIGHLIGHTS

- New PEMFC flow field (FF) designs were developed and tested.
- Experimental analysis of width-scaling parameters in tree-like FF patterns.
- Best design led to PEMFC performances within 11% of a standard serpentine pattern.
- A decrease in FF width-scaling parameters led to improved PEMFC performance.
- Water removal issue was found to be the largest contributor to lower power output.

GRAPHICAL ABSTRACT
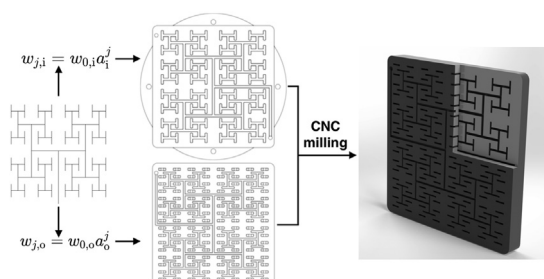
ARTICLE INFO

ABSTRACT

To have a uniform distribution of reactants is an advantage to a fuel cell. We report results for such a distributor with tree-like flow field plates (FFP). Numerical simulations have shown that the width scaling parameters of tree-like patterns in FFPs used in polymer electrolyte membrane fuel cells (PEMFC) reduces the viscous dissipation in the channels. In this study, experimental investigations were conducted on a 2-layer FF plate possessing a tree-like FF pattern which was CNC milled on high-quality graphite. Three FF designs of different width scaling parameters were employed. $I-V$ curves, power curves and impedance spectra were generated at 70%, 60% and 50% relative humidity (25 cm² active area), and compared to those obtained from a conventional 1-channel serpentine FF. It was found that the FF design, with a width scaling factor of 0.917 in the inlet and 0.925 in the outlet

Width scaling factor
Tree-like
Experimental analysis

pattern, exhibited the best peak power out of the three designs (only 11% - 0.08 W/cm^2 lower than reference serpentine FF). Results showed that a reduction of the viscous dissipation in the flow pattern was not directly linked to a PEMFC performance increase. It was found that water accumulation, together with a slight increase in single PEMFC resistance, were the main reasons for the reduced power density. As further improvements, a reduction of the number of branching generation levels and width scaling factor were recommended.

Introduction

Polymer electrolyte membrane fuel cell (PEMFC) systems already contribute to the rapidly growing transition from a fossil fuel-based to a green and renewable energy-based society. A PEMFC is an electrochemical device that uses oxygen and hydrogen in the presence of a catalyst to produce power and water only. A PEMFC stack consists of a series of single cells in which membrane electrode assemblies (MEA) are sandwiched between flow field plates or bipolar plates. A MEA contains the proton exchange membrane, the catalyst layers (electrodes) and the gas diffusion layers (GDL). The cost and efficiency of PEMFC systems still need to be greatly improved for full commercial deployment. Several bodies of authority and organisations have released technological targets for fuel cell stacks and systems [1—3]. A discussion of these targets has been presented by Pollet et al. [4]. One of these targets is, for example, US Department of Energy's cost target of US$40/kW with an efficiency of 65% at peak power and with 12.5 g of platinum (Pt) for 500,000 systems per year, including 80 kW automobiles and 160 kW trucks [1]. The Japanese NEDO's Technology Development Roadmap 2017 has also set high technological targets for PEMFC performance [2]. For example, cell voltages of 0.85 V at 4.4 A/cm^2 and 1.1 V at 0.2 A/cm^2 are targeted by 2040. Such cell voltages can only be reached when all components are optimised in the PEMFC stack, and therefore innovative solutions for current problems need to be proposed and implemented. In Europe, the performance targets focus more on the reduction of the catalyst loading, the system cost and the improvement on durability and general cell volumetric power [3].

In this context, one important target is the optimisation of the flow field plate (FFP), with the important role to (i) evenly distribute the gases at the surface of the electrodes' catalyst layers (CL), (ii) provide good electronic conductivity and (iii) a rigid structural integrity on the MEA. The FFP usually has a specially designed flow field design made of channels to supply the oxygen and hydrogen on both sides of the MEA [5]. It contributes ~60% of the overall mass and represents ~30% of the overall cost of a PEMFC [6]. There are many different ways to design an efficient FFP, however, there is always a compromise in the design, such as having a low pressure drop and at the same time reducing the capabilities of transporting water out of the flow field (see Ref. [7] for a recent review). Iranzo et al. gave an in-depth review of the design trends of biomimetic flow fields [8]. Among the most promising ones are the tree-like or biomimetic flow field patterns, which offer a uniform flow distribution and a desirable change from convective to diffusional flow over the length of the channels; accomplished by the step-wise decrease in channel size [9]. Kjelstrup et al. [10] proposed that the reactants need to be distributed uniformly to minimise the entropy production in the PEMFC. If the reactants are not supplied uniformly, it could cause severe and permanent damage to the MEA's catalyst layers due to fuel starvation [11]. Another advantage of the uniform distribution is that the catalyst utilisation is maximised [12].

Already in 2002, Morgan Fuel Cell Ltd (no longer trading) developed and patented a high-performance flow field pattern called Biomimetic™. This pattern was inspired by animal lungs and plant tissues [13]. Since then, several various approaches have emerged using this type of pattern. Ozden et al. [14] studied different configurations such as variations of leaf- or lung-based designs for the use in direct methanol fuel cells (DMFC). However, these designs turned out to yield the lowest performance when compared to other flow field designs at all operating fuel cell conditions. Behrou et al. [15] proposed a topology optimisation approach for the biomimetic leaf-type FFP based upon maximisation of both output power and homogeneity of the current density distribution. Trogadas et al. [12] presented a lung-inspired flow field pattern, which was 3D printed. They compared different designs with three, four or five branching generation levels of H-formed branches and found that the one with four generations delivered the highest performance. To lower the cost of production, Bethapudi et al. [16] proposed a novel flow field design manufacturing process, adopting a layer-wise printed circuit board (PCB) structure approach. Experiments showed a more stable operation than standard serpentine flow fields with an increase in performance while running the PEMFC with air and at low relative humidity (RH). The design with four generations of H-formed branches was implemented. A similar design with 2-way fractal pathways for the air inlet (4 generations) and air outlet (3 generations) fabricated with PCB plates in a single FFP revealed worse ability for water removal compared to the 1-way design [17].

To date, there have been a few numerical investigations on other biomimetic patterns. Gheorghiu et al. [18] showed that the human lung conforms with Murray's Law and distributes oxygen and carbon dioxide uniformly. Duhn et al. [19]

elaborated a complex shape for inlet and outlet channels for the parallel FFP for solid oxide fuel cells (SOFC), which provided highly uniform reactant distribution between the parallel channels. Hou et al. [20] investigated how the flow changed from convective to diffusional flow. When it comes to the design of a lung-like or tree-like pattern, the scaling was mostly set to conform with Murray's Law [12,16].

Sauermoser et al. [9] recently showed that a change in the width scaling factor (the rate of reduction of the channel width with changing branching generation) away from that of Murray's could have a significant impact on the viscous dissipation. Viscous dissipation is the heat generated due to frictional losses in a flow system. An increase in the width scaling factor showed a reduction in pressure drop along the channels, thus reducing the viscous dissipation. This, in turn, decreased the overall entropy production, which should be beneficial for the PEMFC performance. To consider viscous dissipation in the entropy production only is a simplification, as there are also other sources of dissipation such as thermal or electrical ones. Furthermore, the effect of the pressure drop on the water removal at the outlet branches was not included in the numerical studies. All these additional effects will certainly have an impact on the PEMFC performance. To some degree, we can study one of them apart from the others, however, experiments are required to verify the numerical studies.

Therefore, in this work, we investigated the effect of varying this scaling factor experimentally by changing the flow field channel width, and how it impacted the PEMFC performance. The inlet and outlet pattern's width scaling factor is one of the many optimisation parameters for the tree-like patterns. For example, the distance between the inlet and outlet pattern branches also plays an important role in the forced under-rib convection between the disconnected channels. Due to the complexity of the optimisation of tree-like patterns for use in PEMFCs, it was decided to only focus on the width scaling factor as it relates to our previous studies [9]. To do this, we ran experiments using pure oxygen, to eliminate any issues with fuel/gas starvation effects or gradients under partial pressure conditions. The other objective of this study was to design a flow field, which could be simply machined using traditional CNC milling techniques, capturing still the essential advantage of the tree-like flow field, i.e., the homogenous distribution of reactants and products at small viscous dissipation. Other machining possibilities, such as stamping [5], for improved industrialisation, were not investigated as the main focus of this work was to find possible experimental support for the earlier studies.

In the first section, a brief summary of the theory around the width scaling factors for tree-like flow field patterns (while keeping the cell active area constant) is given, followed by an in-depth description of the newly designed flow fields. In the following section, the experimental setup is described in which different tests are shown. Next, we present the results of the experimental tests performed with the newly designed flow field patterns. The findings are compared to those obtained using an industry-standard, the single-channel serpentine pattern. We also discuss the impact of the scaling factor on the PEMFC performance. In conclusion, we provide an outlook on future developments of FF designs which could lead to improved PEMFC performance.

Theory

Tree-like patterns can be characterised by the following parameters when the channel depths are constant:

1. The width of the channel in the first generation, w_0
2. The depth of the channel, d
3. The maximum number of generations, j_{max}
4. The width scaling parameter, a

In the tree-like pattern, we start to number channels at branching generation level $j = 0$. In addition to the points above, one needs to describe how the length of the channels changes. There are two possibilities for this: a) either the lengths are scaled, like the channel width, or b) manually set to a certain value. In our case, we used the latter option to allow us to serve a square area with feed points. By scaling the length, only a rectangular area could be uniformly filled [9]. The channel width was therefore scaled using the following equation for the inlet (i) and outlet plates (o) (see next section):

$$w_{j,i} = w_{0,i} a_i^j \tag{1}$$

$$w_{j,o} = w_{0,o} a_o^j \tag{2}$$

where $w_{j,i}$ and $w_{j,o}$ are the channel widths at generation j for the inlet and the outlet plate, respectively, and $w_{0,i}$ and $w_{0,o}$ are the channel widths of generation 0 for the inlet and outlet plate, respectively. As already described in the Introduction, our previous work has shown [9] that the entropy production from viscous dissipation (see Eq. (3)) reduces when the width scaling parameter a is increased. In a 1D-system, as used in this section, the viscous dissipation is calculated based upon the pressure drop along the channels, as seen in Eq. (3).

$$\frac{dS_{irr}}{dt} = -\sum_{j=0}^{j_{max}} \sum_{i=1}^{N_j} Q_{j,i} \frac{\Delta p_{j,i}}{T} \tag{3}$$

where $\frac{dS_{irr}}{dt}$ is the total entropy production of the system in J s^{-1} K^{-1}, i is the i-th branch of branching generation level j, N_j is the maximum number of branches at branching generation level j, $Q_{j,i}$ is the volumetric flow rate of branch i in branching generation level j in m^3/s, $\Delta p_{j,i}$ is the pressure drop along branch i in branching generation level j in Pa and T is the uniform temperature of the system. An increase in a leads to larger channels and a lower overall pressure drop along the channels. This decreases the overall entropy production of the system.

In order to avoid having unfeasible or non-machinable patterns, a should be capped at one. Otherwise, the channel width would increase at each branching generation level j. The reason for this is that branches will overlap at a certain point. For the patterns presented below, Equations (1) and (2) was used to calculate the channel widths in the inlet and outlet plate, respectively. As mentioned already, the lengths were set manually.

Experimental

Tree-like flow field plates

Tree-like flow field patterns were CNC milled in Schunk FU4369 graphite plates by HySA Systems Competence Centre, University of the Western Cape, South Africa. The graphite plates had a specific ohmic resistance of 190 $\mu\Omega$m. As previously mentioned, the scope of this study was to design a FFP, machinable with conventional CNC milling techniques. The flow field had, therefore, an inlet and an outlet plate. Three different designs were machined with width-scaling parameters for the patterns in the inlet and outlet plates as shown in Table 1. The table also shows other important parameters, such as the channel width and depth. The sealing of the two FF plates was accomplished by pressing them together with the help of the fuel cell support frame, which also acted as a seal to the environment.

The channel lengths were manually set with the aim to achieve a good coverage of the 25 cm^2 active cell area, cf. Section Theory. The length of generation 1 and 2 was set at 12 mm. After this, the length was set for branching generation level 3 and 4 at 6 mm. This trend, namely reducing the length of the channels by 50% every second branching generation level, was kept until the last generation. The length was always measured from one midpoint of the intersections of two branching generation levels to the next one. For branching generation level 0, the length could only be 23.95 mm, because it needed to be connected to the inlet or outlet hole of the flow field plate, determined by the fuel cell housing. The thickness of the inlet plate was 3 mm, and of the outlet plate 2 mm.

The scaling parameters at the inlet and outlet plate (0.917 and 0.925) were given by limitations in the CNC milling. The smallest cutter was able to mill 0.50 mm. Therefore, the scaling parameter was adjusted so that the branch in the last generation had a channel width of 0.50 mm. The maximum number of branching generations $j_{\max}$ also contained generation 0, hence, the absolute number of branching generations was $j_{\max} + 1$. From the overall nine branching generations of the inlet plate, the last one made the connection to the outlet plate. With this, the connection to the inner layers of the PEMFC's GDL and MEA was obtained. Small rectangular holes connected the two plates with the same width as the branch of the last branching generation of the inlet plate and the width of the previous branching generation. For Design 1 and 2, this means 0.50 mm × 0.55 mm, and for Design 3, 1 mm × 1 mm. Fig. 1a shows Design 3 assembled in the balticFuelCells housing, while Fig. 1c and d shows drawings of

the inlet (Fig. 1c) and outlet (Fig. 1d) plate of Design 3. In addition, Fig. 1b displays a rendered model of the assembled flow field plate of Design 1, to see how the inlet and outlet plates are aligned. The ears included at the inlet plate (Fig. 1c) are used to connect the plate to the fuel cell housing.

Setup

A Biologic FCT-50s test station was used in combination with a balticFuelCells qCF FC25/100 V1.1 LC support frame and a balticFuelCells cellFixture cF25/100 HT Gr. V1.3 fuel cell housing. The single cell PEMFC had an active area of 25 cm^2. The setup was controlled with the software delivered with the FCT-50s. LabVIEW 2019 was used to read the measurements of two thermocouples, which measured the temperatures at the anode and cathode flow fields. The temperature of the fuel cell housing was controlled with a Grant LT Ecocool 100 thermostatic bath, which was connected to the anode and cathode side of the qCF FC25/100 fuel cell support frame. The RH was calculated based on the cell and humidifier temperature, and the gas properties within the Biologic test station software's integrated humidity calculator. The compression of the single-cell was regulated with air, where the pressure was controlled by a FESTO VPPM-6 electrical pressure regulating valve, which was connected to a National Instruments NI USB-6215 for voltage input. This was connected to the LabVIEW software, where the compression was set and measured. A set of two 1 m long 16 mm^2 copper cables were used as load cables. The cell voltage of the PEMFC was measured with a set of two additional high-ohmic sense cables, which were in direct contact with the FFP. Cell temperatures were measured with K-type thermocouples at the anode and cathode flow field plates. The thermocouples were connected to a National instrument Ni 9211. Table 2 gives an overview of the accuracies and resolutions of the equipment used in the experiments.

The reference flow field plate, which was made by balticFuelCells, had a 1-channel serpentine flow field pattern with a channel width and depth of 0.8 mm and a land width of 0.96 mm, milled in graphite with a density of $\geq$1.85 g/cm^3 and a specific resistance of <12 $\mu\Omega$m (through-plane). The reference flow field was always used on the anode side, also in the tests of Designs 1–3. The Designs 1–3 were thus tested as cathode flow fields only. The serpentine FFP had a lower specific resistance than the tree-like designs due to the difference in material. This will be discussed in more detail in Section Comparison of ohmic resistance of the FFPs.

The 5-layer MEA consisted of the following parts: The anode and cathode sides consisted of a Sigracet S28BCE GDL, a cathode and anode with Pt on advanced carbon with a loading of 0.3 mg Pt/cm^2 and 0.1 mg Pt/cm^2 respectively, and a Nafion 212® membrane with a thickness of 50.8 μm. The MEA was purchased completely assembled (hot pressed) from balticFuelCells. Each experiment used the same type of 5-layer MEA.

Pure oxygen (99.999%) and hydrogen (99.999%) were purchased from Linde and used as PEMFC gases. Using pure oxygen reduces the effects of concentration gradients inside the GDL and facilitates the interpretation of the width scaling results. For all experiments using the four types of FF designs, an overpressure of 0.5 bar was set and kept constant.

Table 1 — Parameters of three tree-like flow fields, for the inlet (i) and outlet plates (o). Listed are the width of generation 0, channel depth and generation numbers of the inlet (a_i, $w_{0,i}$, d_i, $j_{\max,i}$) and the outlet (a_o, $w_{0,o}$, d_o, $j_{\max,o}$). Widths and depths are given in mm.

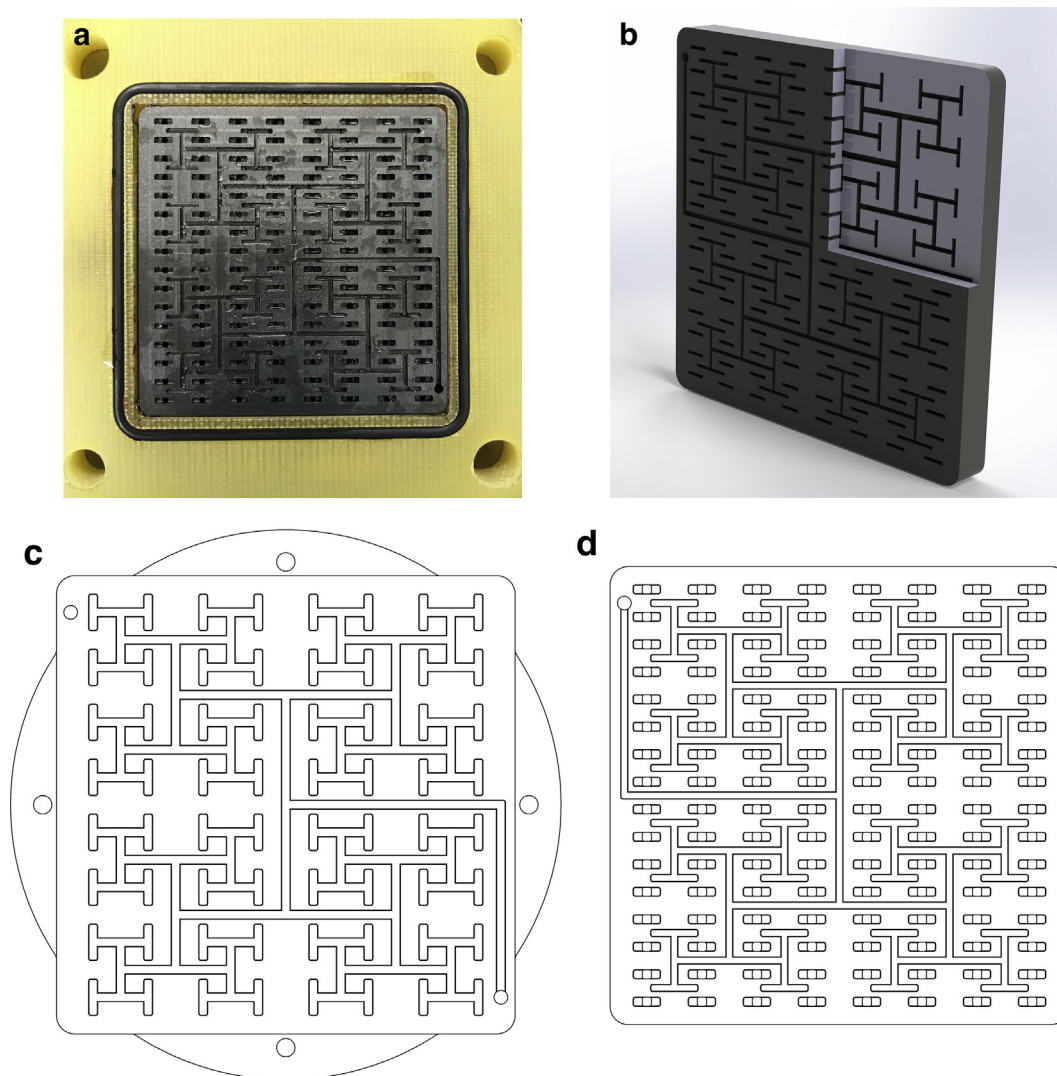| Design	a_i	a_o	$w_{0,i}$ d_i	$w_{0,o}$ d_o	$j_{\max,i}$	$j_{\max,o}$
1	0.917	0.925	1	0.8	8	6
2	0.917	1	1	0.8	8	6
3	1	1	1	0.8	8	6

Fig. 1 — Design 3 assembled in the balticFuelCell housing after experiments (a), render of the assembled flow field plate (Design 1) (b), and drawings of the inlet (c) and outlet (d) plates of Design 3.

Table 2 — Accuracy and resolution information of equipment used in the experiments.

Equipment	Manufacturer	Accuracy	Resolution
FCT-50s	Biologic	Current: 0.5%	Current: 4 mA
		Voltage: <0.1%	Voltage: 76 μV
		Frequency: 1%	
VPPM-6	FESTO	Pressure: 2%	—
NI 9211	National Instruments	Temperature: 0.07 °C	—
NI USB-6215	National Instruments	Voltage: 2690 μV	Voltage: 91.6 μV
LT ecocool 100	Grant	Temperature stability: ±0.05 °C	—

Each newly assembled PEMFC single cell was subjected to the same break-in procedure, which took overall 20 h. The single cell temperature was kept constant at 80 °C, the gas lines for both the anode and cathode were heated at 83 °C. At first, the humidifier temperature was set to 75 °C, which was then reduced to 72 °C after 10 h. The current was slowly ramped up to 35 A, held for 11 h and then reduced to 30 A for the rest of the break-in procedure to avoid a cell voltage drop below 0.4 V. The fuel cell was run in stoichiometric mode with a stoichiometric factor of 2 for hydrogen and 6 for pure oxygen. The high stoichiometric coefficient was chosen to help with the removal of water due to an increase in flow velocities. This was based on the fact that tree-like patterns are prone to water management problems due to low flow rates at the

outlet branches of the pattern [12,16,21,22]. A minimum flow of 200 ml/min for hydrogen and 300 ml/min for oxygen was set.

Each of the following experiments was carried out without a shut-down of the PEMFC. The order of the tests was as follows: Directly after the break-in, the performance test at 70% RH was started. After that, electrochemical impedance spectroscopy (EIS) test was performed, followed by the 3-h hold test. The RH was changed, and then the next performance test was started, with the other two tests following. The same order was then kept for the last RH. Each FFP design was undergoing the same experimental procedures and was tested independently from each other, as a new MEA was used every time the FFP was changed.

Performance test

The performance test procedure followed the European guidelines [23] for testing of automotive MEAs and PEMFCs (see Table 5). The performances of the three new FF designs were measured, and the corresponding $I-V$ and power curves at the three different relative humidities (RH = 70%, 60% and 50%) were generated. The cell temperature was kept constant at approximately 80 °C. The humidifier temperatures were set at 72 °C, 68 °C and 64 °C. The temperature of the heated gas lines, both for the oxygen and hydrogen, was set at 83 °C for all RH settings. Stoichiometric flow settings were used, with a stoichiometric factor of 2 for hydrogen and 6 for oxygen. Gas flow rates had a minimum value of 200 ml/min for hydrogen and 300 ml/min for oxygen. If the cell voltage had not equilibrated itself, the current was kept constant until it stayed the same within ±5 mV for the recommended data acquisition time. The cell voltage measurements were then averaged over the last 30 s of each current step.

Electrochemical impedance spectroscopy test

Three different currents, 7.5 A, 15 A and 22.5 A, were used during the EIS procedure for each RH and flow field pattern employed. An amplitude around the mentioned base values of ±5% was set. The frequency was decreased from 10 kHz to 0.1 Hz. A minimum flow of 84 ml/min for hydrogen and 126 ml/min for oxygen, with a stoichiometric factor of 2 for hydrogen and 6 for oxygen was used. The cell temperature was set at 80 °C, the line temperature at 83 °C and the humidifier temperature between 72 °C and 64 °C, according to the RH (see Section Performance test). Before each of the three currents was tested, the fuel cell was equilibrated for 2 min. The data was then analysed with the EC lab, followed by a circuit fitting procedure performed in MATLAB 2019.

Circuit fitting

Circuit fitting was performed in MATLAB with the help of the open-source code from Dellis [24]. To allow for a better comparison of the fitted parameters, upper and lower boundaries were set within the MATLAB code. A modified Randles circuit (see Fig. 5 top left), taken from Dhirde et al. [25] was used for the circuit fitting. R_1 represents the ohmic resistance of the fuel cell in Ohm (Ω). The first parallel loop describes the process at the anode, whereas the second one describes the After

that, electrochemical impedance equivalent at the cathode. A constant phase element (CPE) was used in the circuit fitting because the semi-circles were depressed at high frequencies [26]. The CPE uses two parameters, namely a time constant Q in F cm^2 s$^{\alpha-1}$ and an exponent of phase angle α. The R_2 and R_3 are charge transfer resistances at the anode and cathode, respectively, in Ω. R_2 and R_3 were summed up to calculate the overall charge transfer resistance in the PEMFC, R_{ct}. Additionally, a Warburg (W) convective diffusion element was used, where we had a diffusion resistance R_d in Ω and a time constant τ_d in s [26].

Because the Warburg convective diffusion element has two fitting parameters, a diffusion impedance Z_d was calculated with the equation below (Eq. (4)). This allowed for an easier comparison of the values between the different EIS tests.

$$Z_d = R_d \frac{\tanh \sqrt{\tau_d j \omega}}{\sqrt{\tau_d j \omega}} \tag{4}$$

where ω is the angular frequency in 1/s, and j is the imaginary unit. After calculating Z_d, the absolute value $|Z_d|$ was taken for comparison.

Hold test

During the hold test, which was started right after the EIS test, a current of 20 A was applied and held for 3 h. The cell temperature was kept at 80 °C, the line temperature at 83 °C and the humidifier temperature between 72 °C and 64 °C, depending upon the RH (see Section Performance test). The same settings regarding gas flow rates as in the EIS test procedure were used.

Results and discussion

The results of the three tests carried out on the four flow field plates setups will be reported in the same order as described above.

Performance tests

Fig. 2a and b shows the results of the performance tests for all four flow fields and three RH values. The standard deviation was on average ± 0.3 mV, with a maximum of 4 mV, which occurred at the last current step of Design 3. It can be observed from the $I-V$ and power curves that the serpentine pattern had the best performance, independent of RH. Additionally, higher current densities could be reached with the serpentine pattern than Design 1 to 3. The tree-like flow field plate designs, however, were in the best case (Design 1, 70% RH), able to achieve a maximum power density, only 11% (0.08 W/cm^2) lower than the reference one. In the worst case, a reduction of 37% (0.26 W/cm^2) was observed. Reducing the width scaling factor in both the inlet and outlet patterns led, therefore, to a performance increase. This has not been experimentally shown before to the best of our knowledge. Between 0 and 0.6 A/cm^2, all tree-like patterns exhibited higher cell voltages compared to those obtained for the serpentine pattern. One of the reasons for this could be due to the uniform distribution of
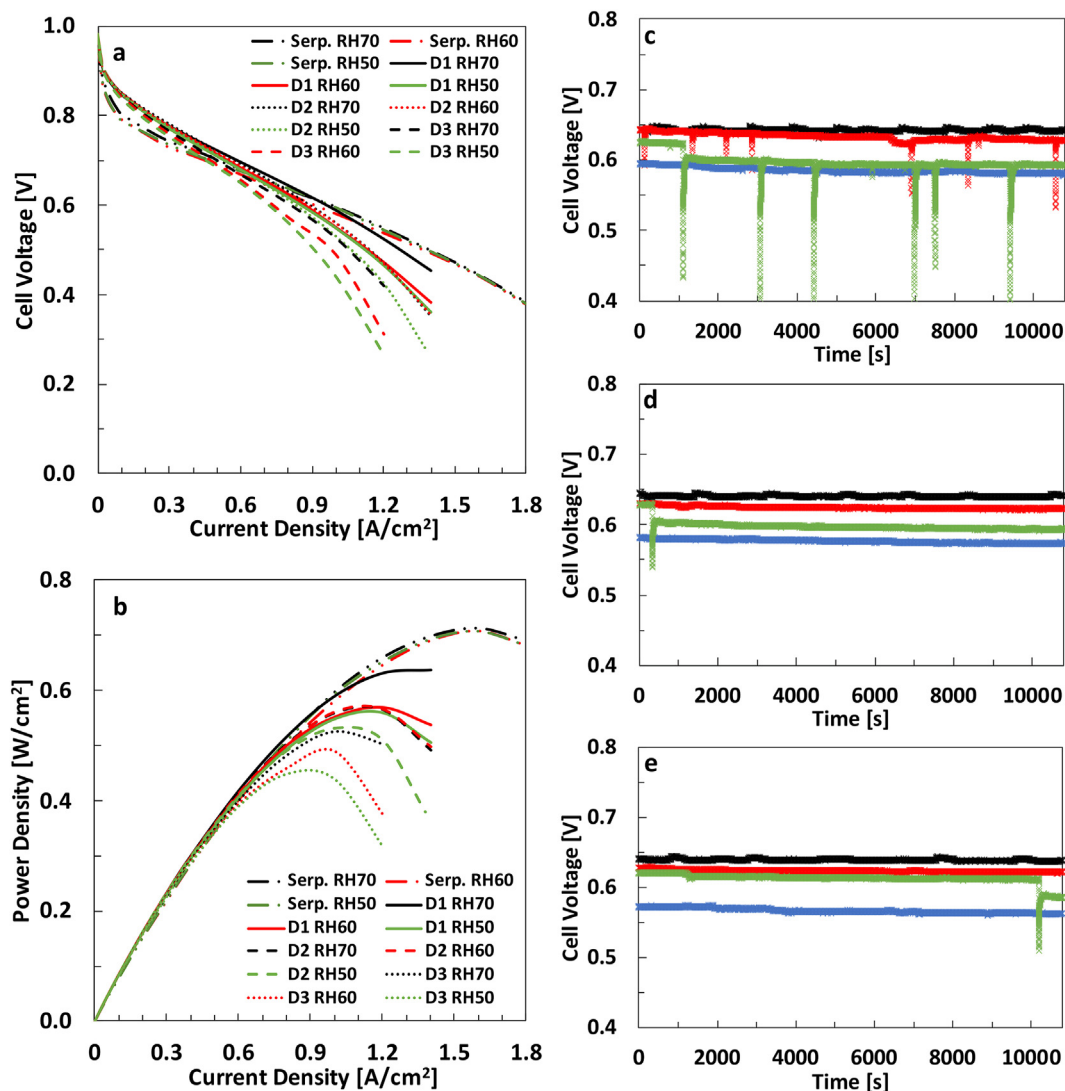
Fig. 2 — *I*—*V* curves (a) and power curves (b) for all four flow field plate setups at 70%, 60%, and 50% RH. Results of hold tests for the serpentine pattern (black), Design 1 (red), Design 2 (green) and Design 3 (blue) at 70% (c), 60% (d), and 50% (e) RH. (For interpretation of the references to colour in this figure legend, the reader is referred to the Web version of this article.)

the fuel across the catalyst layer, which in turn increases catalyst utilisation [12]. However, the advantage of this uniformity steadily decreased with an increase in current density, leading to lower PEMFC performances compared to the reference pattern. The reasons for this are discussed in the next section.

Among the new flow field designs, Design 1 had the best performance, especially at 70% RH. The pattern with no width scaling ($a_i = a_o = 1$) was clearly worse. The performance tests for Design 3 for all three RH values were interrupted at 1.2 A/m², because the cell voltage did not reach a steady-state.

Electrochemical impedance spectrum tests

Figs. 3 and 4 show the results of the EIS tests for all FF setups and RH values, in the form of Nyquist plots from 10 kHz to 0.1 Hz at 7.5 A, 15 A and 22.5 A. Data appeared to

be regular with only a few outliers, mostly in the high-frequency region of the Nyquist plot. At first glance, an immediate difference could be seen between the results of the serpentine FFP (Fig. 3a) and the three new designs (3b, 4a and 4b). Tree-like FFs had a distinct second semi-circle at lower frequencies at all currents and RH values. The serpentine FF (Fig. 3a) had only a very small one at high currents (22.5 A), indicating no significant mass transfer limitations explained by the use of pure oxygen at high stoichiometries. The small second semi-circle size slightly decreased with a decrease in RH, as there was less water in the system, which could cause problems with *e.g.*, flooding. When looking at the first semi-circle, at higher frequencies, it can be observed that the size (radius) of it, was relatively constant at 7.5 A for all FF designs. The same applies to 15 A. At 22.5 A, however, a significant increase in radius for both Design 2 (Figs. 4a) and 3 (Fig. 4b) at all RH values was observed, showing significant losses due to mass transfer
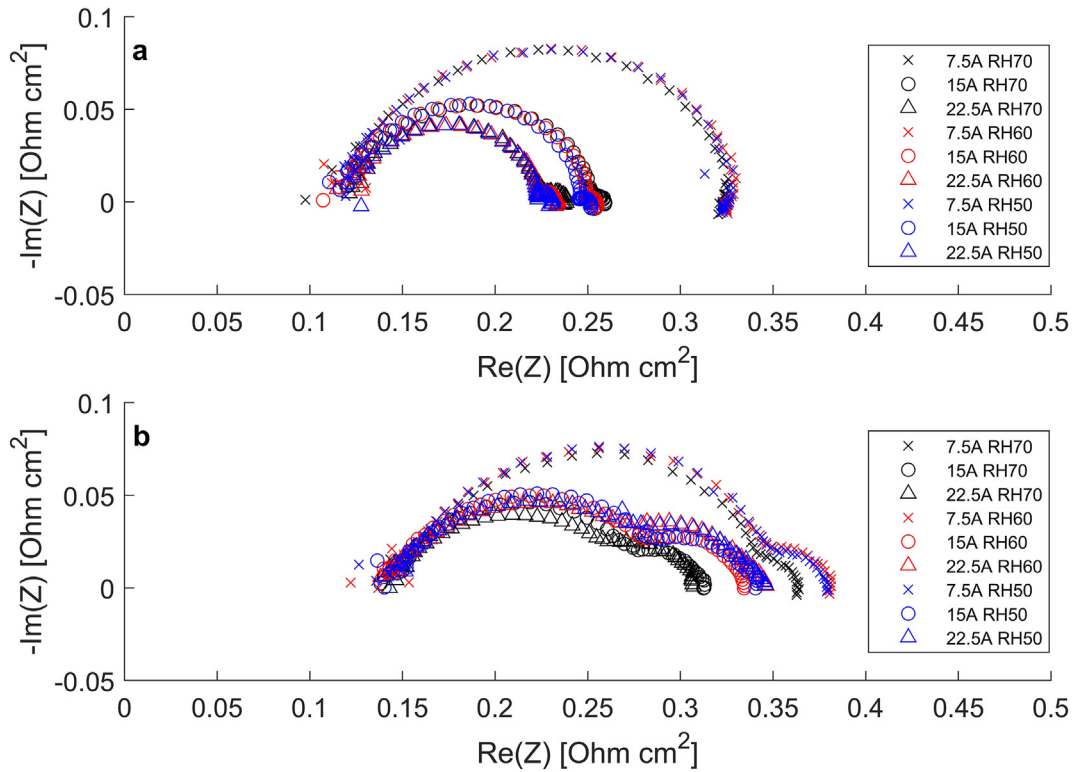
Fig. 3 − Nyquist plots of the EIS tests for serpentine pattern (a) and Design 1 (b) at 7.5 A, 15 A, and 22.5 A and 50%, 60%, and 70% RH.
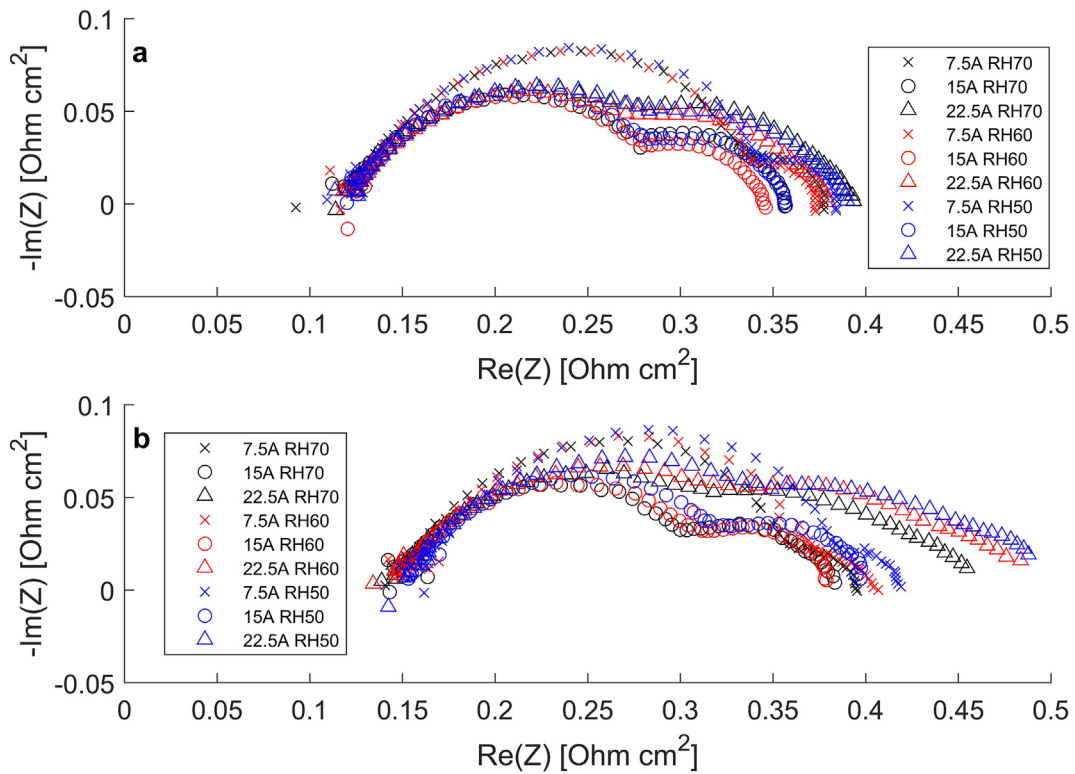

Fig. 4 − Nyquist plots of the EIS tests for Design 2 (a) and Design 3 (b) at 7.5 A, 15 A, and 22.5 A and 50%, 60%, and 70% RH.

limitations. For Design 1 (Fig. 3b), only the test at 70% RH exhibited a size comparable to the serpentine pattern.

This could help explain the performance drop at lower RH settings during the performance tests. When changing the RH, the shape of the EIS curves did not significantly change for the serpentine pattern. However, for the tree-like patterns, in some cases, large deviations in the size of the semi-circles were observed compared to the serpentine pattern.

Each Nyquist plot (Figs. 3 and 4) on its own showed that the intersections with the real axis at different RH settings were situated near the same position. We can, therefore, assume that the membranes were hydrated properly, even at lower RH values. Another point was that the intersection of the EIS measurements with the real axis occurred at a higher real value for Designs 1 and 3, compared to the serpentine pattern and Design 2. This is further discussed in the next section, when we investigate the ohmic resistance of the PEMFC R_1 from the circuit fitting procedure, as the noise of the EIS measurements at the highest frequencies (10 kHz and slightly below) made it difficult for interpretation based on the Nyquist plots.

Circuit fitting

Fig. 5a to c shows the result of the circuit fitting for all four FF design setups and three RH settings. On average, a R^2 value of 0.986 was achieved with the circuit fitting.

As already mentioned above, the Nyquist plots for Designs 1 (Fig. 3b) and 3 (Fig. 4b) showed an intersection with the real axis at a higher value than the serpentine pattern (Fig. 3a) did. The same variation was observed in the fitted parameter R_1 (Fig. 5a) *i.e.*, the ohmic resistance of the PEMFC. The pattern with a scaling factor of 1 for both inlet and outlet plate (Design 3) had wider channels, and therefore an increased channel:-land ratio compared to Design 1. This results in a slightly higher resistance of the flow field plate and to a smaller contact area with the GDL leading to a higher contact resistance. Design 2, however, showed ohmic resistances similar to the serpentine pattern. This variation was counter-intuitive and not a circuit fitting issue, as evident from the Nyquist plot. The scaling factor of 1 at the outlet plate of Design 2, instead of 0.925 in Design 1, led to a higher channel:land ratio on the outlet plate, same as for Design 3, increasing the FFP bulk resistance. Hence, an in-depth analysis of the ohmic bulk resistances of the different designs was conducted to investigate the decrease in R_1 of Design 2 compared to Design 1 (which can be found in Section Comparison of ohmic resistance of the FFPs).

Looking at the overall charge transfer resistance R_{ct} (Fig. 5b), the following trends could be observed: At 7.5 A, R_{ct} did not vary much between the tested designs and RH values (R_{ct} was between 8.1 mΩ and 9.3 mΩ). Increasing the current to 15 A reduced R_{ct} further for all experiments, fitting well with the theory behind the charge transfer resistance [27]. However, for Design 3, the decrease was marginal. At 22.5 A, an increase in R_{ct} was reported for Design 2 (max. 8.3 mΩ) and 3 (max. 12.8 mΩ), corresponding to the fast decay in cell voltage, as seen in Fig. 2a. For Design 1, this was seen only at 50% and 60% RH (max. 6.6 mΩ). For the measurement at 70% RH, Design 1 showed the same trend as for all experiments with the serpentine pattern, namely, a decrease in R_{ct} down to 5.3 mΩ.

We assume that the increase in R_{ct} while increasing the current from 15 A to 22.5 A of the serpentine pattern at 60% RH was due to the curve fit, as no additional cell voltage drop was reported in the I–V curves compared to 70% and 50% RH. The increase in R_{ct} reported for Design 1 to 3 could be indicative of water flooding restricting the reactant flow to the catalyst layer, according to Fouquet et al. [26] and agreeing with the reduction in PEMFC performance compared to the serpentine pattern. Issues related to water management in the PEMFC are further discussed in Section Water management.

The absolute Warburg diffusion impedance $|Z_d|$, gives an estimate of the mass transport resistances in the PEMFC. At high frequencies, the oxygen molecules do not need to move far, thus decreasing the impedance [27]. Therefore, we primarily looked at the results at 0.1 Hz, the lowest tested frequency (Fig. 5c). It was observed that the tree-like pattern had an order of magnitude higher Warburg impedance compared to the reference one. According to Fouquet et al. [26], the Warburg diffusion resistance changes significantly when flooding occurs in the catalyst layer. This leads to an increase in $|Z_d|$, and agrees with our observations.

Direct comparison with EIS data from Trogadas et al. [12] or Bethapudi et al. [16,17] was rather difficult due to the different operating parameters. However, results from Bethapudi et al. [16] showed that the biomimetic patterns exhibited no distinct second semi-circle, as well as lower charge and mass transfer resistances. This was due to the contribution of the uniform reactant and water distribution. In contrast, the serpentine pattern exhibited a semi-circle starting at 600 mA/cm^2, indicating mass transfer limitations due to the use of air [16]. In the presented experiments, the serpentine design did not display this distinct second semi-circle due to the use of pure oxygen at a high stoichiometric coefficient. Again, this shows that our FF design, despite the uniform reactant distribution of tree-like patterns, had restrictions regarding fuel transport to the catalyst layer. These restrictions are assumed to be caused by water flooding, which is discussed in Section Water management.

Hold tests

The objective of the hold test was to study the long-term performance of the new FFP designs. Results are shown in Fig. 2c, d and e for the serpentine pattern (black), Design 1 (red), Design 2 (green) and Design 3 (blue) at 70% (Figs. 2c), 60% (Fig. 2d), and 50% (Fig. 2e) RH. Table 3 gives values for the mean cell voltages V in V and their standard deviations σ in mV for the different experiments. The tests were immediately performed after the EIS test. Generally said, and as expected, an improvement of cell voltage stability with a decrease of RH was observed, as shown by the reduction in σ. At 70% RH, all four flow field plate setups showed cell voltage drops and unstable behaviours, also shown by the highest σ values in Table 3. Especially Design 2 had voltage drops of more than 0.2 V. Another interesting fact was that Design 2 had a sudden drop in cell voltage either at the start or at the end of the test. This could be related to either a sudden event of water flooding or the blockage of several outlet channels of the inlet pattern. However, as the hold test experiments indicated
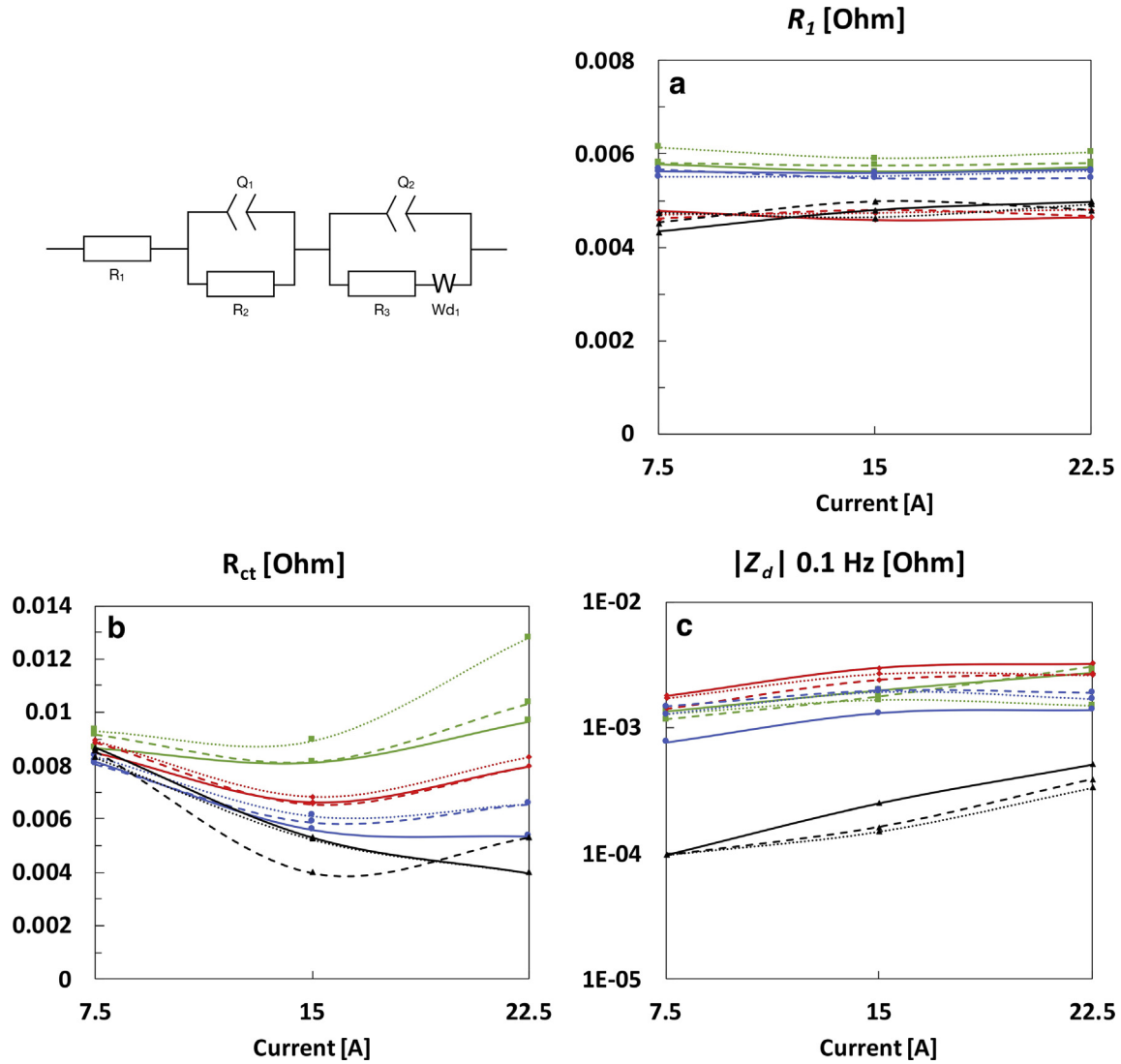
Fig. 5 – Results of the circuit fitting using the modified Randles [25] circuit (top left) for the serpentine pattern (black), Design 1 (blue), Design 2 (red), and Design 3 (green) at 70% (solid line), 60% (dashed line), and 50% (dotted line) RH. R_1 (a) is the ohmic resistance of the cell, R_{ct} (b) is the overall charge transfer resistance in the PEMFC, and $|Z_d|$ (c) is the absolute Warburg diffusion impedance calculated with Eq. (4) at 0.1 Hz. (For interpretation of the references to colour in this figure legend, the reader is referred to the Web version of this article.)

Table 3 – Mean voltages V in V and standard deviations σ in mV of the 3 h hold test experiments for each FFP design and RH settings.						
	RH70		RH50		RH50	
	$\bar{V}$ [V]	σ [mV]	$\bar{V}$ [V]	σ [mV]	$\bar{V}$ [V]	σ [mV]
Serp	0.642	1.7	0.641	1.1	0.640	1.3
D1	0.633	5.1	0.624	1.9	0.624	1.6
D2	0.596	12.9	0.598	6.3	0.613	7.2
D3	0.585	4.1	0.577	2.5	0.567	3.5

(Fig. 2c–e, green data points), these blockages were cleared before the next hold test experiment at a lower RH. At this stage and based upon our data, we do not have a clear explanation of why Design 2 behaved differently than the other tree-like designs. This will be the subject of our next study. The difference in width scaling factor should not cause this disparity, as it would then show in some form in the hold test experiment results of either Design 1 or 3. Design 3 showed no significant cell voltage drops. However, the cell voltage constantly decreased over the course of the 3-h experiment at all three RH settings. Design 3, even though it showed the lowest mean cell voltage of all FFPs, had the most stable cell voltage profile compared to Design 1 and 2 at 70% RH with a σ of 4.1 mV. At 50% RH, Design 1 was the most stable tree-like pattern (σ of 1.6 mV). If we look directly at the cell voltage jumps, it seems that the cell voltage profile of Design 1 was even smoother than the serpentine one. Despite the lower cell voltages of the tree-like patterns, it was shown during the hold test experiments that the tree-like patterns, mostly Design 1, were able to deliver stable cell voltages at lower RH conditions, which was a promising result.

Water management

As documented in Section Performance tests, it can be observed that the tree-like FFs in the best case (Design 1, 70% RH) may come within 11% to the performance of the serpentine flow field. The promise of the presented tree-like FFPs is their uniform flow distribution [9]. Supplying fuels in a uniform way helps to avoid local concentration gradients and, therefore, additional overpotential losses. Even though pure oxygen was used on the cathode side to reduce mass transfer limitations caused by low oxygen partial pressures, the Warburg diffusion impedance (Fig. 5c) of the tree-like designs was one order of magnitude higher than with the serpentine flow field. Therefore, a resistance against the gas transport to the catalyst layer must have been created, for example, by a water blockage of pores inside the GDL [28]. Such blocks are known to decrease the reaction rate at the electrodes [29]. The reduction of PEMFC performance in connection with water accumulation inside the PEMFC while using tree-like patterns has been reported already earlier [12,16,17,21,22]. Cho et al. [30] showed already that lung-like flow fields, which are similar to the presented designs, have problems with water removal in the small branches of the pattern due to limited convection due to low flow rates. These low flow rates can lead to the blockage of outlet branches in the inlet pattern, leading to a non-uniformity of the fuel distribution and lower PEMFC performance due to the non-availability of fuel at various regions of the catalyst layer, diminishing the main advantage of the newly presented designs. This could be related to the increase in R_{ct} for the tree-like designs (except Design 1 at 70% RH).

Trogadas et al. [12] and Bethapudi et al. [16] used a scaling factor for their channel dimensions according to Murray's Law, which delivers a smaller a than the one used in the presented designs. This leads to higher pressure drops, as shown in Ref. [9], further helping with the water removal. In connection with the use of straight channels for the water removal, this can be the reason for the better performance of the lung-inspired patterns proposed by Trogadas et al. [12] and Bethapudi et al. [16] when compared to standard serpentine patterns. The effect of a higher pressure drop was also seen in the presented tree-like designs. Design 1 had a ~6% higher pressure drop than Design 2, and a ~9% higher one than Design 3, which seemed to improve the water removal as indicated by the higher performance. The pressure drops were calculated with the hydraulic diameter approach, as discussed in Ref. [9].

The hold tests at 50% and 60% RH (Fig. 2d and e) did not show any sharp cell voltage drops, meaning that the water accumulation was very steady over time as no sudden blockage of channels and the followed spikes of cell voltage occurred. It could also be seen that changing the RH had no significant impact on the results of the performance (Fig. 2a and b) and EIS (Figs. 3 and 4) test performed with the serpentine flow field. As the intersection with the real axis of the Nyquist plot did not change with RH, proper membrane hydration can be therefore assumed. This could also be said about presented tree-like flow fields. However, the higher charge transfer resistances (Fig. 5b) and Warburg diffusion impedances (Fig. 5c) indicated problems, most probably caused by poor water management [26]. Even though a reduction in RH reduces the amount of water transported into the PEMFC, charge transfer resistances increased, and the Warburg diffusion impedance stayed approximately the same. An explanation for this could be that the tests of each design were started at the highest RH. Therefore, water was able to accumulate and stayed inside the cell even during the tests at lower RH, thus further showing that the tree-like designs had problems with water removal.

Cho et al. [31] proposed the use of capillaries in the flow field plate to facilitate better water removal to help with water management. Trogadas et al. [21] implemented laser engraved capillaries based on a particular lizard's skin in a tree-like FFP, showing significant performance improvements. These concepts could be implemented in future work to improve the performance of the presented designs further.

Comparison of ohmic resistance of the FFPs

In order to evaluate the impact of the ohmic bulk resistance of the FFPs, simulations on the plates were performed using COMSOL 5.5. For this, the 3D model created in SOLIDWORKS 2019 were used and meshed by applying the physics-controlled mesh algorithm with the element size set to fine on the imported STL file from SOLIDWORKS 2019. The EC physics module was used for the simulations. The ground was set at the face of the FFP, which touches the GDL in the PEMFC, and the terminal was set at the opposite surface. The model was isothermal, and the electric current was the only flux in the system. The standard settings for the stationary, direct solver were used, which uses the MUMPS algorithm and a relative tolerance of 0.001. Results were computed for currents between 0 and 30 A using a parametric sweep. As a consistency check, the surface average of the normal current density on the terminal side was calculated and compared to the set current. Because the serpentine FFP, supplied by balticFuelCells, consisted of a different material than the tree-like designs, a fifth simulation was created. Here, the serpentine FFP had the same material as the presented designs. The resistance was calculated by creating a global evaluation of the resistance R_{11}, which is directly provided by COMSOL 5.5, see Table 4. This resistance is the ohmic bulk resistance of each FFP, further called R_{bulk}.

Simulation results showed coherent values for different current densities, with an error between 10^{-13} and 10^{-14} in the above-described consistency check. Due to the lower specific resistance (12 $\mu\Omega$m) of the serpentine FFP, the calculated ohmic resistance was much lower than in the tree-like designs, which were machined into Schunk FU4369 graphite (190

Table 4 — Electric bulk resistance (R_{bulk}) values for the serpentine pattern (Serp.), the three presented designs (D1, D2, and D3) and the serpentine pattern if the same material as for Design 1 to 3 would be used (Serp.*).

	Serp.	D1	D2	D3	Serp.*
$R_{bulk}[m\Omega]$	0.027	0.429	0.434	0.473	0.432

$\mu\Omega$m). The resistance of the FFP increased with an increase in scaling factor a_i and a_o, due to the increase in channel width and, therefore, a reduction in the contact area. However, if the serpentine pattern used the same material as the tree-like designs, it was observed that Design 1 exhibited a smaller resistance, even though the design had two patterns and two plates (inlet and outlet pattern). If the scaling factor would decrease even further, the resistance would decrease too.

By calculating the cell voltage drop at a current density of 1.2 A/cm^2 with Ohm's Law, we could see that the R_{bulk} had only a minor contribution to the overall PEMFC performance and was not the cause for the lower cell voltages of the tree-like designs. For Design 1 to 3, this cell voltage drop was between 0.51 and 0.57 mV, whereas it was around 0.03 mV for the serpentine pattern. Hence, we can conclude that varying the width scaling factor and thus the channel:land ratio of the tree-like patterns had no major contribution to the cell voltage drops caused by the electric bulk resistance of the FFP. Comparing the bulk resistances R_{bulk} with R_1 from the circuit fitting (Fig. 5a) led to the observation that the ohmic resistance R_{bulk} (Table 4) of the flow field plate was only a small part of R_1.

The reason for the lower R_1 of Design 2 compared to Designs 1 and 3 could be that the two plates of the tree-like flow field plate (inlet and outlet plate) had a better "MEA-plate" and "plate-plate" contact (i.e. a lower contact resistance) in Design 2 than 1 or 3, as we used the same clamping pressure in all of our experiments and assumed proper membrane hydration. The improved contact between the plates in Design 2 could be due to machining tolerances of the CNC milling, which could directly impact contact resistance.

iR-corrected $I-V$ curves (Fig. 6) were generated for each FFP design at 70% and 50% RH to investigate the impact of R_1 on the PEMFC performance. For each FFP and RH conditions, R_1
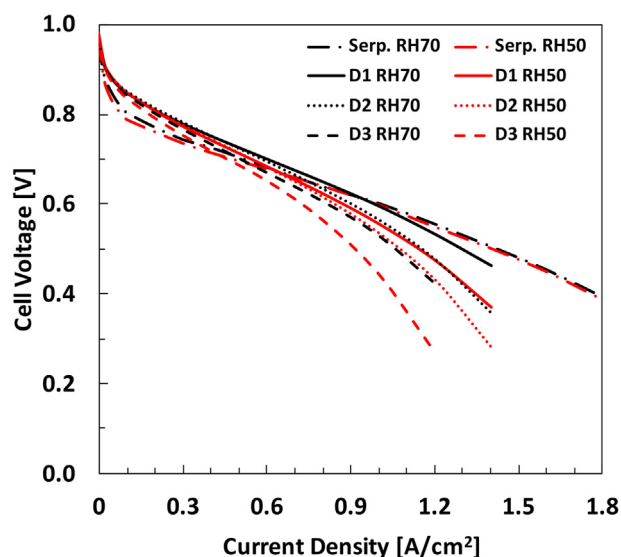
from the circuit fitting was averaged over the three tested currents (7.5 A, 15 A and 22.5 A). Afterwards, the voltage drop for the iR-correction was calculated using Ohm's Law. Due to minor changes in R_1 with changing current as seen in Fig. 5a and the measurement noise at high frequencies, this approximation appeared to be acceptable enough. Fig. 6 shows that the difference in R_1 did not account for the large disparity between the performances of the different designs. Furthermore, assuming that mass transfer limitations are the main contributor to the lower cell voltages for the tree-like designs is still holding, as the tree-like designs still displayed lower performances compared to those obtained with the serpentine pattern. This observation was due to a sharp non-linear decline in cell voltage beyond 0.5 A/cm^2. Fig. 6 also indicates that if mass-transfer limitations or problems caused by water accumulation would be fixed in Design 1, its performance could be higher than the one from the serpentine pattern, especially at 70% RH.

Comparison to numerical analysis

The next point for discussion is the comparison between the numerical analysis of the width scaling factors of such tree-like FFPs [9]. It was shown earlier that an increase in width scaling factor, in our case a_i and a_o, decreased the viscous dissipation, increasing thereby the efficiency of the FFP. In the study presented in Ref. [9], only hydrodynamic pressure losses were included. The experiments showed that a decrease in viscous dissipation in the flow channels of the flow field did not automatically increase the fuel cell performance. This topic is much more complex, as a higher pressure drop also helps with the removal of water [32]. This was observed in the experiments, as Design 1 had the highest performance among the tree-like designs. It is well known that there is an essential dissipation also from ohmic and thermal sources. This creates a trade-off situation, which can be handled by *Pareto optimisation* and should be added to future numerical analyses of these patterns. The presented results showed that using the entropy production based upon the viscous dissipation alone was not enough to use it as a design tool for the optimisation of tree-like patterns in PEMFCs, as major phenomena such as water blockage of channels were not included.

Influence of channel:land ratio and width scaling factor

A final point for discussion is the ratio between channels and land on the flow field. For serpentine patterns, it had been shown that a channel:land width ratio around 1 showed improved PEMFC performance at the cost of high pressure drops [33]. Due to the increased pressure drop when this ratio is decreased, an optimum can be found if the total efficiency (including the PEMFC and auxiliary equipment like pumps) is investigated [33]. For the case of the presented tree-like patterns, we calculated the overall channel:land ratio based upon the surface coverage of the channels on the outlet plate. Design 1 had a lower channel:land ratio (~0.25) at the outlet plate than Design 3 (~0.46) but had a higher power output, indicating that decreasing the channel:land ratio far below 1 improved the PEMFC performance. We saw that similar conclusions regarding this ratio known from the serpentine

Fig. 6 – IR-corrected $I-V$ curves using R_1 from the circuit fitting at 70% (black) and 50% RH (red) for serpentine pattern (dash-dotted), Design 1 (solid), Design 2 (dotted) and Design 3 (dashed). (For interpretation of the references to colour in this figure legend, the reader is referred to the Web version of this article.)

pattern were difficult to apply directly to tree-like patterns. One reason might be due to the changing channel widths of the tree-like patterns, which requires the use of the surface coverage for the channel:land ratio instead of using the channel and land width.

To further reduce the width scaling factor seems to give a promising possible improvement of the PEMFC performance, as indicated by the performance tests (Section Performance tests). However, there is a trade-off situation here. The decrease of a_i or a_o will lead to smaller channel widths at higher branching generation levels. This could lead to increased problems with water removal, as shown by Trogadas et al. [12] and Trogadas and Coppens [22]. However, in Refs. [12,22], the description of the narrower channels combined with an increase in water problems was related to an increase in branching generation levels and, therefore, a reduction in flow velocity in the outlet branches. Suppose the number of generation levels stays constant, a decrease of width scaling factor would increase flow velocity in the branches connected to the MEA. As described by Cho et al. [30], the limited convection due to low flow velocities was one of the causes for the poor water removal of tree-like patterns, thus, higher velocities should be more beneficial.

Influence of branching generation numbers

The number of branching generation levels also has an impact on the PEMFC performance [12,22,34]. We used a different approach in counting the branching generation levels. However, if the same one as Trogadas et al. [12] was used, we would be at four branching generation levels. Cho et al. [34] reported that there is an optimum number of generation levels. The main reasons for increasing the generation level number is the accompanying shift to a diffusion-dominated flow, as expressed by a Peclet number smaller than one at the outlets of the tree-like pattern, and a more uniform reactant distribution [12,34]. However, there is a diminishing return at a certain point. The increase in PEMFC performance flattens out with a further increase in the number of generation levels. Therefore, future work should include the design of a pattern with an optimal number of generation levels combined with a varying width scaling factor to investigate the effect of changing channels sizes.

Conclusions

The PEMFC performance of three tree-like flow fields at the cathode side, with different design rules for channel width, was investigated. The flow field plates consisted of two CNC machined graphite plates; one served as the oxygen inlet distributor, the other one as water outlet collector, allowing for a uniform oxygen distribution over the 25 cm^2 area MEA.

With $j = 9$ generations of branches, a channel length reduction of 50% every second branching generation, and a width scaling factor a_i equal to 0.917 and a_o equal to 0.925, a power density was obtained within 11% of the value of a standard serpentine flow field at a RH of 70%. This was a remarkable result, as the presented tree-like FFPs were the first iteration of our design, without any additional optimisation. The iR-corrected $I-V$ curves indicated that resolving the mass transfer limitations could possibly lead to higher PEMFC performances than those obtained with the serpentine pattern. In addition, it may be an advantage that the hold test experiments indicated stable cell voltages without any major potential drops for Designs 1 and 3. Water accumulation seemed to be steady when no sudden cell voltage drops occurred at lower RH.

The differences in performance of the presented designs were investigated by further analysing the EIS data and holding test experiments. In the absence of oxygen concentration gradients due to pure oxygen being used on the cathode, impedance spectroscopic data further suggested that the present tree-like flow field had a rate-limiting step at the cathode reaction not present with the serpentine flow field. This was shown by an increase in the Warburg diffusion impedance and overall charge transfer resistance, assumed to be caused by water accumulation and blockages. As discussed, it may be possible to reduce this resistance by tailoring the water management of the whole system.

We further reported that numerical analyses of tree-like patterns should not only use the viscous dissipation as the optimisation criterion. Lowering the pressure drop (viscous dissipation) alone did not automatically yield higher PEMFC performance. However, it could help reduce parasitic losses due to lower demands on the auxiliary equipment such as the gas supply system. This was seen in the experiments as an increase in width scaling parameter a_i and a_o did not cause the PEMFC to perform better. Therefore, Pareto frontiers for a multi-criteria optimisation should be used in future numerical optimisations to include the different trade-offs.

Declaration of competing interest

The authors declare that they have no known competing financial interests or personal relationships that could have appeared to influence the work reported in this paper.

Acknowledgements

Appendix

Table 5 shows the current steps done during the performance tests. This was taken from Tsotridis et al. [23].

Table 5 — This table shows the different set points during the performance tests and their according dwell and data acquisition times.

Set point no.	Current [A]	Current Density [A/cm^2]	Dwell Time [s]	Data acquisition time [s]
1	0	0.00	60	30
2	0.5	0.02	60	30
3	1	0.04	60	30
4	1.5	0.06	60	30
5	2	0.08	60	30
6	2.5	0.10	60	30
7	5	0.20	$\geq$120	30
8	7.5	0.30	$\geq$120	30
9	10	0.40	$\geq$120	30
10	15	0.60	$\geq$120	30
11	20	0.80	$\geq$120	30
12	25	1.00	$\geq$120	30
13	30	1.20	$\geq$120	30
14	35	1.40	$\geq$120	30
15	40	1.60	$\geq$120	30
16	45	1.80	$\geq$120	30
17	40	1.60	$\geq$120	30
18	35	1.40	$\geq$120	30
19	30	1.20	$\geq$120	30
20	25	1.00	$\geq$120	30
21	20	0.80	$\geq$120	30
22	15	0.60	$\geq$120	30
23	10	0.40	$\geq$120	30
24	7.5	0.30	$\geq$120	30
25	5	0.20	$\geq$120	30
26	2.5	0.10	60	30
27	2	0.08	60	30
28	1.5	0.06	60	30
29	1	0.04	60	30
30	0.5	0.02	60	30
31	0	0.00	60	30

REFERENCES

[1] U. D. of Energy. Cost Projections of PEM Fuel Cell Systems for automobiles and Medium-Duty Vehicles. www.energy.gov. [Accessed 18 August 2020].

[2] New Energy and Industrial Technology Development Organization. NEDO's Technology development Roadmap for fuel cells and hydrogen. https://www.nedo.go.jp/library/battery_hydrogen.html. [Accessed 31 January 2020].

[3] Fuel Cells and Hydrogen 2 Joint Undertaking Fch 2 Ju. Addendum to the multi-annual work plan 2014—2020. https://www.fch.europa.eu/sites/default/files/MAWP%20final%20version_endorsed%20GB%2015062018%20%28ID%203712421%29.pdf. [Accessed 31 January 2020].

[4] Pollet BG, Kocha SS, Staffell I. Current status of automotive fuel cells for sustainable transport". Current Opinion in Electrochemistry 2019;16:90—5. https://doi.org/10.1016/j.coelec.2019.04.021.

[5] Hamilton PJ, Pollet BG. Polymer electrolyte membrane fuel cell (PEMFC) flow field plate: design, materials and characterisation. Fuel Cell 2010;10(4):489—509. https://doi.org/10.1002/fuce.201000033.

[6] Li X, Sabir I. Review of bipolar plates in PEM fuel cells: flow-field designs. Int J Hydrogen Energy 2005;30(4):359—71. https://doi.org/10.1016/j.ijhydene.2004.09.019. fuel Cells.

[7] Sauermoser M, Kizilova N, Pollet BG, Kjelstrup S. Flow field patterns for proton exchange membrane fuel cells. Frontiers in Energy Research 2020;8:13. https://doi.org/10.3389/fenrg.2020.00013.

[8] Iranzo A, Arredondo C, Kannan A, Rosa F. Biomimetic flow fields for proton exchange membrane fuel cells: a review of design trends. Energy 2020;190:116435. https://doi.org/10.1016/j.energy.2019.116435.

[9] Sauermoser M, Kjelstrup S, Kizilova N, Pollet BG, Flekkøy EG. Seeking minimum entropy production for a tree-like flow-field in a fuel cell. Phys Chem Chem Phys 2020;22(13):6993—7003. https://doi.org/10.1039/C9CP05394H.

[10] Kjelstrup S, Coppens M-O, Pharoah JG, Pfeifer P. Nature-inspired energy- and material-efficient design of a polymer electrolyte membrane fuel cell. Energy Fuels 2010;24(9):5097—108. https://doi.org/10.1021/ef100610w.

[11] Taniguchi A, Akita T, Yasuda K, Miyazaki Y. Analysis of electrocatalyst degradation in PEMFC caused by cell reversal during fuel starvation. J Power Sources 2004;130:42—9. https://doi.org/10.1016/j.jpowsour.2003.12.035.

[12] Trogadas P, Cho JIS, Neville TP, Marquis J, Wu B, Brett DJL, Coppens M-O. A lung-inspired approach to scalable and robust fuel cell design. Energy Environ Sci 2018;11(1):136—43. https://doi.org/10.1039/C7EE02161E.

[13] Synnogy Ltd. The UK fuel cell industry: a capabilities guide. https://www.lowcvp.org.uk/assets/reports/Fuel Cell UK CapabilityGuide_100903.pdf. [Accessed 18 August 2020].

[14] Ozden A, Ercelik M, Ouellette D, Colpan CO, Ganjehsarabi H, Hamdullahpur F. Designing, modeling and performance investigation of bio-inspired flow field based DMFCs. Int J Hydrogen Energy 2017;42(33):21546—58. https://doi.org/10.1016/j.ijhydene.2017.01.007.

[15] Behrou R, Pizzolato A, Forner-Cuenca A. Topology optimization as a powerful tool to design advanced PEMFCs flow fields. Int J Heat Mass Tran 2019;135:72—92. https://doi.org/10.1016/j.ijheatmasstransfer.2019.01.050.

[16] Bethapudi V, Hack J, Trogadas P, Cho J, Rasha L, Hinds G, Shearing P, Brett D, Coppens M-O. A lung-inspired printed circuit board polymer electrolyte fuel cell. Energy Convers Manag 2019;202:112198. https://doi.org/10.1016/j.enconman.2019.112198.

[17] Bethapudi VS, Hack J, Trogadas P, Hinds G, Shearing PR, Brett DJ, Coppens MO. Hydration state diagnosis in fractal flow-field based polymer electrolyte membrane fuel cells using acoustic emission analysis. Energy Convers Manag 2020;220:113083. https://doi.org/10.1016/j.enconman.2020.113083.

[18] Gheorghiu S, Kjelstrup S, Pfeifer P, Coppens M-O. Is the lung an optimal gas exchanger? In: Losa GA, Merlini D, Nonnenmacher TF, Weibel ER, editors. Fractals in biology and medicine. Basel: Birkhäuser; 2005. p. 31—42. https://doi.org/10.1007/3-7643-7412-8.

[19] Duhn J, Jensen A, Wedel S, Wix C. Optimization of a new flow design for solid oxide cells using computational fluid dynamics modelling. J Power Sources 2016;336:261—71. https://doi.org/10.1016/j.jpowsour.2016.10.060.

[20] Hou C, Gheorghiu S, Coppens M-O, Huxley VH, Pfeifer P. Gas diffusion through the fractal landscape of the lung: how deep does oxygen enter the alveolar system? In: Losa GA, Merlini D, Nonnenmacher TF, Weibel ER, editors. Fractals in biology and medicine. Basel: Birkhäuser; 2005. p. 17—30. https://doi.org/10.1007/3-7643-7412-8_2.

[21] Trogadas P, Cho JI, Bethapudi VS, Shearing P, Brett D, Coppens MO. Nature-inspired flow-fields and water management for PEM fuel cells. ECS Transactions 2020;98(9):145—52. https://doi.org/10.1149/09809.0145ecst.

[22] Trogadas P, Coppens M-O. Nature-inspired electrocatalysts and devices for energy conversion. Chem Soc Rev 2020;49(10):3107—41. https://doi.org/10.1039/C8CS00797G.

[23] Tsotridis G, Pilenga A, Marco GD, Malkow T. EU harmonised test protocols for PEMFC MEA testing in single cell configuration for automotive applications; JRC Science for Policy report. EUR 27632 EN 2015. https://doi.org/10.2790/54653.

[24] Dellis J-L. Zfit. https://www.mathworks.com/matlabcentral/fileexchange/19460-zfit. [Accessed 18 August 2020].

[25] Dhirde AM, Dale NV, Salehfar H, Mann MD, Han T. Equivalent electric circuit modeling and performance analysis of a PEM fuel cell stack using impedance spectroscopy. IEEE Trans Energy Convers 2010;25(3):778–86. https://doi.org/10.1109/TEC.2010.2049267.

[26] Fouquet N, Doulet C, Nouillant C, Dauphin-Tanguy G, Ould-Bouamama B. Model based PEM fuel cell state-of-health monitoring via ac impedance measurements. J Power Sources 2006;159(2):905–13. https://doi.org/10.1016/j.jpowsour.2005.11.035.

[27] Yuan X-Z, Song C, Wang H, Zhang J. Electrochemical impedance spectroscopy in PEM fuel cells: fundamentals and applications. Springer, London: Ch. EIS Equivalent Circuits; 2010. p. 139–92. https://doi.org/10.1007/978-1-84882-846-9_4.

[28] Pérez-Page M, Pérez-Herranz V. Study of the electrochemical behaviour of a 300 W PEM fuel cell stack by Electrochemical Impedance Spectroscopy. Int J Hydrogen Energy 2014;39(8):4009–15. https://doi.org/10.1016/j.ijhydene.2013.05.121.

[29] Jayakumar A, Sethu SP, Ramos M, Robertson J, Al-Jumaily A. A technical review on gas diffusion, mechanism and medium of PEM fuel cell. Ionics 2015;21(1):1–18. https://doi.org/10.1007/s11581-014-1322-x.

[30] Cho J, Neville T, Trogadas P, Meyer Q, Wu Y, Ziesche R, Boillat P, Cochet M, Manzi-Orezzoli V, Shearing P, Brett D, Coppens M-O. Visualization of liquid water in a lung-inspired flow-field based polymer electrolyte membrane fuel cell via neutron radiography. Energy 2019;170:14–21. https://doi.org/10.1016/j.energy.2018.12.143.

[31] Cho JI, Neville TP, Trogadas P, Bailey J, Shearing P, Brett DJ, Coppens MO. Capillaries for water management in polymer electrolyte membrane fuel cells. Int J Hydrogen Energy 2018;43(48):21949–58. https://doi.org/10.1016/j.ijhydene.2018.10.030.

[32] Arvay A, French J, Wang JC, Peng XH, Kannan AM. Nature inspired flow field designs for proton exchange membrane fuel cell. Int J Hydrogen Energy 2013;38(9):3717–26. https://doi.org/10.1016/j.ijhydene.2012.12.149.

[33] Chowdhury MZ, Genc O, Toros S. Numerical optimization of channel to land width ratio for PEM fuel cell. Int J Hydrogen Energy 2018;43(23):10798–809. https://doi.org/10.1016/j.ijhydene.2017.12.149.

[34] Cho JI, Marquis J, Trogadas P, Neville TP, Brett DJ, Coppens MO. Optimizing the architecture of lung-inspired fuel cells. Chem Eng Sci 2020;215:115375. https://doi.org/10.1016/j.ces.2019.115375.